Materials Horizons

ROYAL SOCIETY OF CHEMISTRY

COMMUNICATION

View Article Online
View Journal | View Issue

Check for updates

Cite this: *Mater. Horiz.*, 2026, **13**, 1448

Received 16th July 2025,
Accepted 14th October 2025

DOI: 10.1039/d5mh01359c

rsc.li/materials-horizons

Leveraging solid–liquid interaction to fabricate drug-microsphere in site encapsulated bone-repair scaffolds

Fengxin Zhao,[a] Puxin Liu,[a] Xinyi Wang,[a] Jirong Yang,*[bc] Changshun Ruan,*[bc] Dongxiao Li,[d] Xiangdong Zhu,[a] Yumei Xiao*[a] and Xingdong Zhang[a]

Drug-encapsulated scaffolds are crucial to treat challenging bone defects, but the approach for loading drugs into scaffolds is limited. Despite microspheres as carriers that improve drug efficacy and the therapeutic window, the traditional "first preparation – then encapsulation" in drug-microsphere encapsulated scaffolds remains complicated and time-consuming. Herein, we present a facile approach for fabricating drug-microsphere in site encapsulated bone-repair scaffolds (CHP@Drug), in which a solid–liquid interaction triggered by vortex oscillation can be leveraged to realize in site preparation and simultaneous encapsulation of drug-loaded microspheres, rapidly and uniformly. Owing to the induced collision, homogenized and reinforced shear stress from the solid–liquid interaction, CHP@Drug endowed a sustained drug release and an interconnected porous structure. As a proof of concept, CHP@Drugs, were loaded with three drugs respectively, demonstrating significantly enhanced healing of critical-sized, infected, and osteoporotic bone defects *in vivo*. This study offers a facile and universal way to load drugs into tissue-repair scaffolds, with in-clinic potential.

New concepts

We present a facile method to fabricate drug-encapsulated scaffolds in a continuous, rapid, and time-saving process, breaking through the limitation of the traditional "first preparation – then encapsulation" method. Moreover, CHP@Drugs were flexibly designed for the repair of challenging bone defects. Notably, the induced collision as well as homogenized and reinforced shear stress is created from the solid–liquid interaction, triggered by vortex oscillation in just 40 s, which allows uniform drug-loaded PLGA microspheres in site preparation and simultaneous encapsulation within CHP@Drugs, resulting in the stable and sustained drug release of CHP@Drug. This study advances the design approach of scaffolds for challenging bone repairs and overcomes the complicated and time-consuming preparation of the drug-microsphere encapsulated bone-repair scaffold. Offering a facile, rapid, and efficient fabrication of CHP@Drugs for the enhanced repair of challenging bone defects, and a universal approach to fabricate drug-microsphere encapsulated scaffolds for other tissue repair.

Introduction

Challenging bone defects that cannot spontaneously heal, *e.g.*, large-sized, osteoporotic, and infected bone defects, remain difficult problems in clinic.[1–4] The difficulty is mainly attributed to the severely damaged surrounding tissues and pathological microenvironment, thus the development of effective external interventions is necessary for accelerating their reconstruction.[5,6] Administering specific drugs to ameliorate the surrounding microenvironment is a robust approach for therapy of challenging bone defects.[7] However, systemic administration of drugs often results in low bioavailability at the site of the bone defect.[7–9] Drug-encapsulated scaffolds have been developed to realize precise and localized intervention protocols, enhancing therapeutic efficacy.[9,10] In addition, scaffolds with elaborate designs play a crucial role in promoting the repair of bone defects.[1,11] Therefore, developing a drug-encapsulated scaffold as the local-delivery platform capable of adapting the specific drug to meet the requirements for challenging bone defects, holds significant clinical value.[12]

Many approaches for the fabrication of a drug-encapsulated scaffold have been explored to meet these clinical demands over the past few decades.[12–14] Direct encapsulation of drugs into scaffolds is a common and simple approach.[7,15,16] The absence of interaction between scaffolds and drugs leads to burst release, making it challenging to maintain prolonged drug delivery within a safe and effective concentration range for

[a] *National Engineering Research Center for Biomaterials, College of Biomedical Engineering, Research Center for Material Genome Engineering, Sichuan University, Chengdu, 610065, China. E-mail: xymzl2000@126.com*
[b] *Research Center for Human Tissue and Organ Degeneration, Institute of Biomedical and Biotechnology, Shenzhen Institute of Advanced Technology, Chinese Academy of Sciences, Shenzhen, 518055, China. E-mail: jr.yang@siat.ac.cn, cs.ruan@siat.ac.cn*
[c] *University of Chinese Academy of Sciences, Beijing, 100049, China*
[d] *Sichuan Academy of Chinese Medicine Science, Chengdu, Sichuan, 610042, China*

the repair process.[9,17] To address this, the strategies that augment interactions between scaffolds and drugs, such as electrostatic interactions, hydrogen bonding, and reversible covalent bonds (*e.g.*, Schiff base bonding, disulfide bonding), have been employed.[18–22] However, these approaches necessitate tailored modification of both drugs and scaffolds to optimize their interaction based on their physicochemical properties,[7,23,24] often leading to complex synthetic procedures, potential generation of by-products, and a possible reduction in drug activity.[25–28] Moreover, modified drugs require re-evaluation before clinical application, and these strategies are not universally applicable to the sustained release of the various drugs used in treating challenging bone defects.

Drug-microsphere encapsulated scaffolds have gained popularity for repairing challenging bone defects. This approach allows a flexible selection of drugs based on the specific bone defect scenario,[29–31] avoiding the need for drug and scaffold modification. Microspheres as carriers to pre-load various drugs can be encapsulated in scaffolds to improve the therapeutic window and possess the broad availability of materials, such as gelatine, hyaluronic acid, poly(lactic-*co*-glycolic acid), *etc.*[32,33] Emulsification utilizing immiscible oil and aqueous solutions to generate droplets, is a widely used method for microsphere preparation due to its simple equipment requirements, low cost, scalability, and versatility.[34,35] Whereas, the traditional ''first preparation – then encapsulation'' of drug-microsphere encapsulated scaffolds involves multiple steps, including emulsion preparation, microsphere collection, washing, encapsulation, and scaffold construction, making it cumbersome, intermittent, and time-consuming.[29,36,37] In addition, the uniformity of microspheres, which significantly affects drug loading and release profiles, should be controlled by the emulsification process.[38,39] To achieve the uniform size distribution of microspheres, it is necessary to modify the emulsification method and/or add emulsifiers.[40–42]

Here, we propose an in site encapsulated approach for facile fabrication of drug-microsphere bone-repair scaffolds (CHP@Drug), in which a solid–liquid interaction can be leveraged to realize in-site preparation and simultaneous encapsulation of drug-loaded microspheres, rapidly and uniformly (Scheme 1). The solid–liquid system is established based on micro-hydroxyapatite (μHAp), methacrylate anhydride-modified collagen (CMA) and poly(lactic-*co*-glycolic acid) (PLGA) combined with specific drugs. The solution of methacrylate anhydride-modified collagen (CMA), an essential component of natural bone, not only serves as the basis of the scaffold but also provides an aqueous solution for in site emulsification and rapid polymerization. The PLGA solution contained specific drugs (PLGA@Drug, oil solution), and was then dropped into CMA (aqueous solution) to form the drug-loaded PLGA microspheres (PMD). The oil and aqueous solutions mix was referred to as the liquid phase, with the solid–liquid interaction between μHAp (solid phase) and CMA/PLGA (liquid phase) triggered by a simple one-pot vortex oscillation. The induced collision as well as homogenized and reinforced shear stress is created from the solid–liquid interaction, and the resulting microspheres exhibit exceptional uniformity, endowing stable and sustained release of drugs. Additionally, as a proof of concept, the CHP@Drugs was loaded with three specific drugs, for repairing three kinds of challenging bone defects in rats, including critical-sized, infected, and osteoporotic bone defects, underscoring the system's versatility and clinical potential.

Results and discussion

Continuous and rapid fabrication of CHP@Drug

The CHP@Drug, which simultaneously integrated the drug-delivery system and biomimetic scaffold, was continuously and rapidly fabricated *via* leverage of solid–liquid interaction triggered by a simple method of one-pot vortex oscillation (Fig. 1A). During the preparation process, the PLGA@Drug solution was subjected to in site PMD under a vortex oscillation of just 40 s. The mixed solutions of CMA and μHAp are not only used as pivotal components in biomimetic scaffolds but also as the polymerizable aqueous solution (CMA) and solid phase (μHAp). Subsequently, the mixture was cured for 90 s, PMD was in site encapsulated in the CHP@Drug hydrogel, which was then lyophilized to remove organic solvents, yielding the CHP@Drug. As shown in Fig. 1B, the PMD was dispersed in a porous network structure of CHP@Drug and CP@Drug (without μHAp). Notably, the statistical results in Fig. 1C demonstrated that the PMD in the CHP@Drug was more uniform in size than that in the CP@Drug. In addition, the CHP@Drug surface displayed more porous structures which exhibited an interconnected porous structure compared to the CH@Drug without PMD (Fig. 1D and E), attributed to the volatilization of organic solvents which dissolved PLGA. The porosity of the scaffold can be tuned by adjusting the freeze-drying process and the proportion of organic solvents used.[43,44] Furthermore, *in vivo* infiltration experiments show that interconnected porous structures had a faster cell infiltration rate, and a higher tissue infiltrated area compared to the CH@Drug (Fig. 1F, G and Fig. S1A). Consistent with the widely recognized optimal pore size range of 100 to 350 μm for effective bone regeneration, both the surface and internal porosity of CHP@Drug scaffolds fell within this favourable window.[45] The interconnected porous structures facilitated fluid exchange inside and outside the scaffold as well as early cellular infiltration, crucial for effective bone repair.[46] Although the porous structure has a detrimental impact on the mechanical properties of the scaffolds, the porous structure on the surface did not affect the mechanical properties of the CHP@Drug (Fig. S1B), owing to the PLGA microspheres acting as a reinforcing phase to enhance the mechanical properties of the scaffolds.[47] In addition, the water absorption ratio of the CHP@Drug showed that it could quickly hydrate in a short period (30 min), reaching about 300% (Fig. S1C). The results suggest that the CHP@Drug can rapidly hydrate following implantation, which would facilitate cellular infiltration, the transport of nutrients, and the diffusion-release of the drug.[48]

Taken together, the CHP@Drug was prepared successfully in a continuous, rapid, and time-saving process. Moreover, the

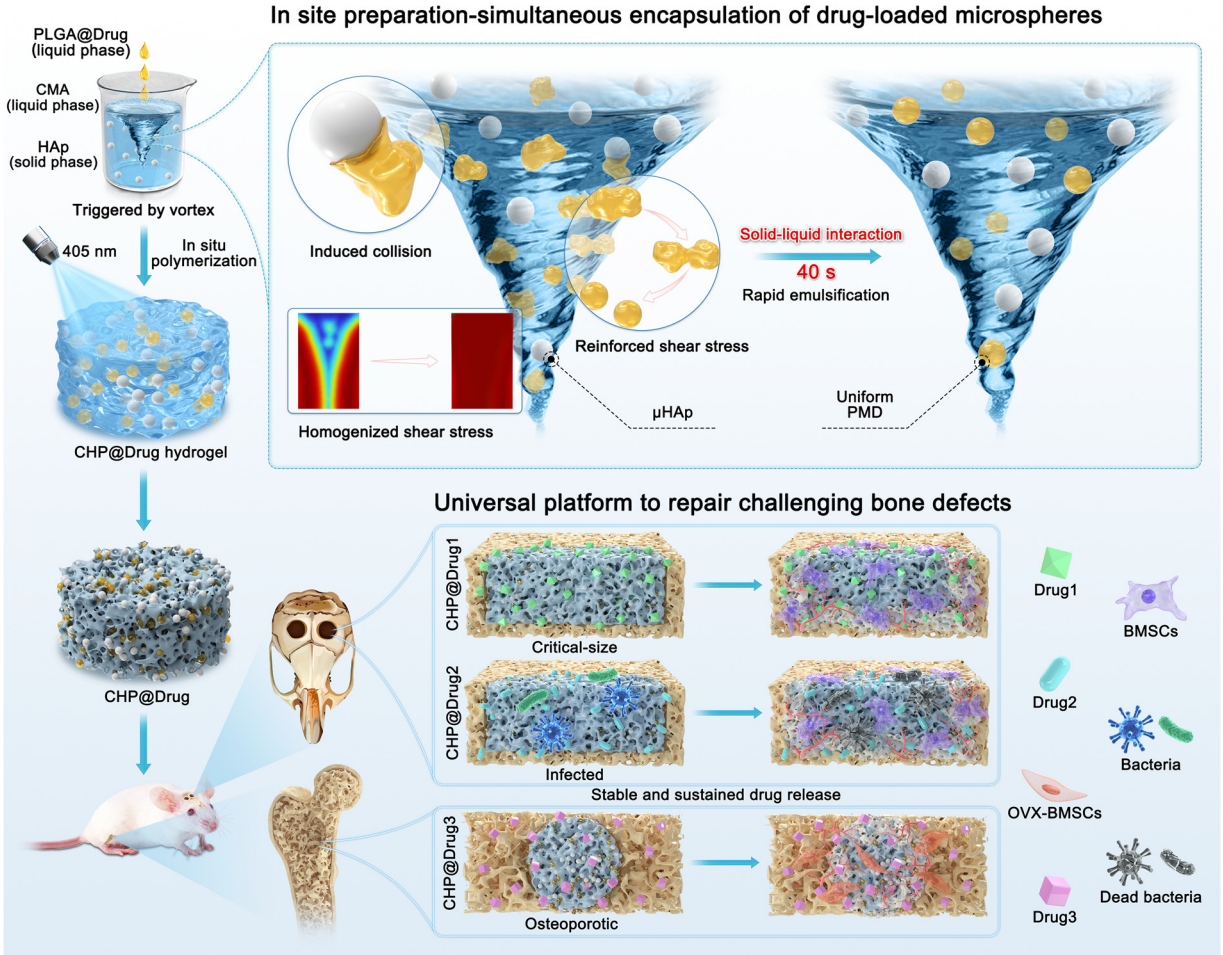

Scheme 1 Schematic illustration of the facile approach for the fabrication of drug-microsphere in site encapsulated bone-repair scaffolds (CHP@Drug) and its application for challenging bone defects. A solid–liquid interaction between μHAp and CMA/PLGA is triggered by vortex oscillation, which contributes to induced collisions between μHAp and PLGA@Drug droplets, creating homogenized and reinforced shear stress of the liquid phase to break PLGA@Drug droplets (PMD) into smaller and more uniform droplets.

interconnected porous structures of the scaffold were beneficial to cellular infiltration which is critical to bone repair. Interestingly, owing to the solid–liquid interaction between μHAp and CMA/PLGA, the uniform PMD was also achieved without use of any emulsifier. This approach simplifies the complicated preparation process of drug-microsphere encapsulated scaffolds as reported in previous studies, where the process involved multiple steps, including emulsion preparation, solvent evaporation, microsphere collection, microsphere washing, microsphere encapsulation and scaffold construction.[29,36]

The formation of PMD *via* leverage of solid–liquid interaction

To investigate the influence of the solid–liquid interaction on the uniformity of PMD within the CHP@Drug, as shown in Fig. 2A, a series of CHP@Drugs were respectively fabricated with varying μHAp content (0, 25, 50, 100, and 200 mg mL^{-1}). PLGA microspheres are used for loading a diverse array of drugs with varying solubility properties (*e.g.*, in dichloromethane–DCM, water, and dimethyl sulfoxide–DMSO) to apply in the multiplicity of causal factors in challenging bone defects.[38,49] DCM is typically employed as the solvent for PLGA. Drugs dissolved in DCM, water, and DMSO were respectively added to the PLGA solution to obtain three oil phases: drug dissolved in PLGA solution, drug–PLGA immiscible solution and drug–PLGA miscible solution. To visualize the PMD within CHP@Drugs, three types of fluorescent molecules representing drugs with different solubility properties were used: Nile red (dissolved in DCM), FITC-labelled poly-L-lysine (PL-FITC, dissolved in water), and Icariin (dissolved in DMSO).

Fluorescent molecules labelled PMD were collected by degrading the scaffolds. As illustrated in the fluorescence images in Fig. 2B and Fig. S2, the PMD in the μHAp0 group exhibited a discrete particle size distribution including some larger and some smaller particles. However, the uniformity of the PMD was elevated with the gradual increase of μHAp's solid content in three liquid phases. The kernel density plots were employed to illustrate the overall distribution of PMD particle sizes and their predominant size ranges of different scaffolds in Fig. 2C and Fig. S3A, C. The horizontal span of the kernel density plot decreased with increasing μHAp content,

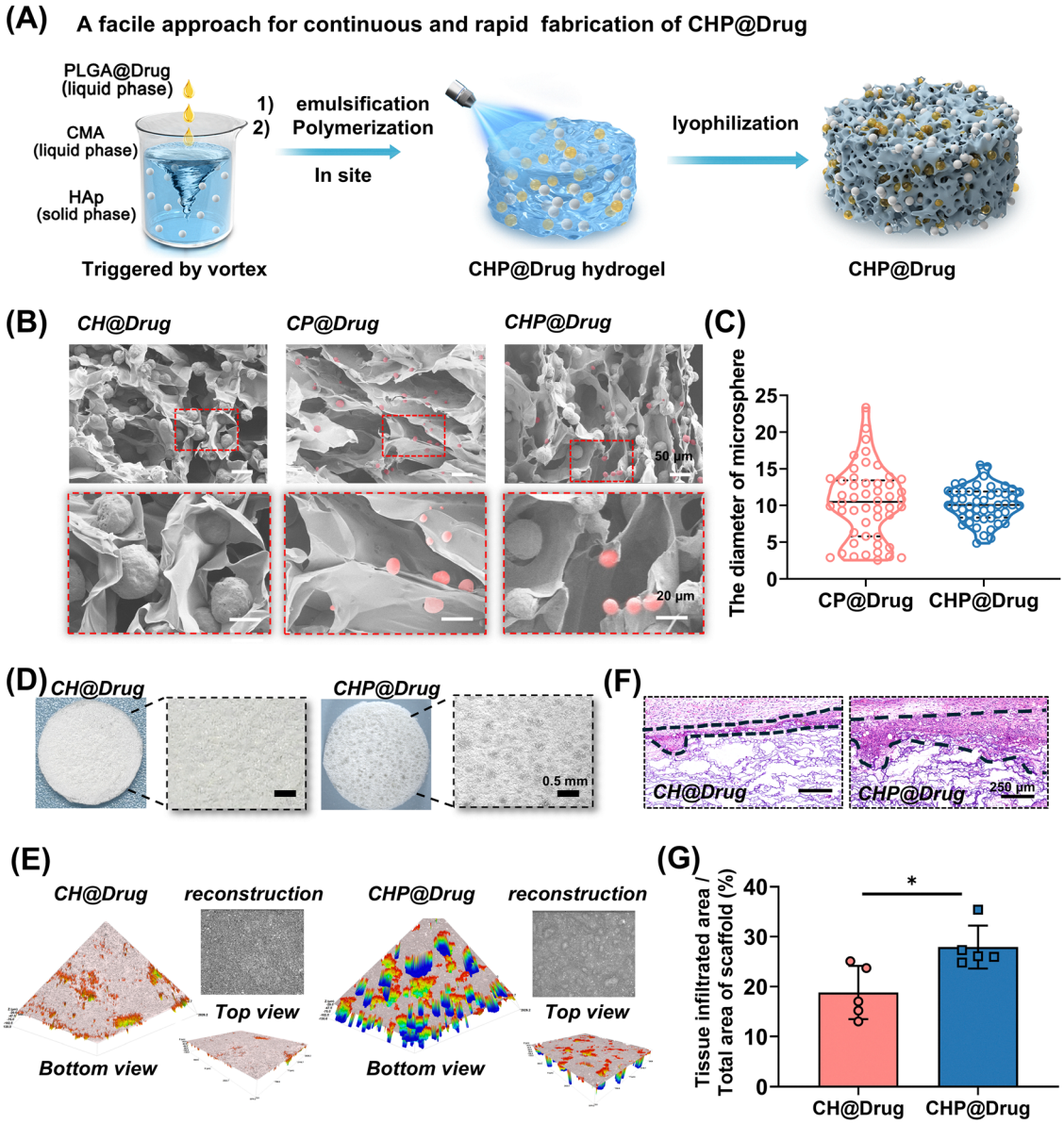

Fig. 1 The properties of CHP@Drug. (A) A facile approach for continuous and rapid fabrication of CHP@Drug *via* leverage of solid–liquid interaction. (B) SEM images of CH@Drug (without PLGA microspheres), CP@Drug (without μHAp) and CHP@Drug. (C) The quantitative analysis of the diameter of PMD in the CP@Drug and CHP@Drug from SEM images (n = 50). (D) and (E) Stereomicroscope and 3D optical profiler images of the CH@Drug and CHP@Drug. (F) H&E staining and (G) statistical results (n = 5) of tissue infiltration in the CH@Drug and CHP@Drug implanted into the subcutaneous of rats after 7 days.

indicating a greater convergence of microsphere size distributions and a reduction in anomalous size. The peaks in Fig. 2C and Fig. S3A, C progressively concentrated within a narrower range, and the number of smaller particle sizes was significantly lower in the other groups compared to μHAp0. The box plot further demonstrated the distribution of microsphere size (Fig. 2D and Fig. S3B, D). The μHAp0 group exhibited a notable discrepancy between the median and the mean, with a relatively small lower quartile. The median was skewed toward the lower quartile, suggesting a wider distribution of microsphere sizes and a greater proportion of smaller microspheres in this group. As the content of μHAp increased, the upper and lower quartiles in the box became closer, and the median and mean values converged more closely. To better illustrate the distribution of microsphere sizes, the ratio of median to mean (P) and the quartile deviation (Q) were defined (Fig. 2E and Fig. S4A). The P-value represents the overall distribution of sizes, where smaller ratios indicate a higher proportion of smaller microspheres. The Q-value reflects the degree of data dispersion, with smaller differences indicating a higher degree of convergence. The μHAp0 group has the lowest P-value and the highest Q-value among all the groups. With the increase of μHAp solid content, the P-value fluctuated only in a small range, while the Q-value gradually decreased, and a good degree of convergence was achieved at 100 mg mL^{-1}. In all, these results demonstrate that the introduction of solid phase HAp significantly enhances

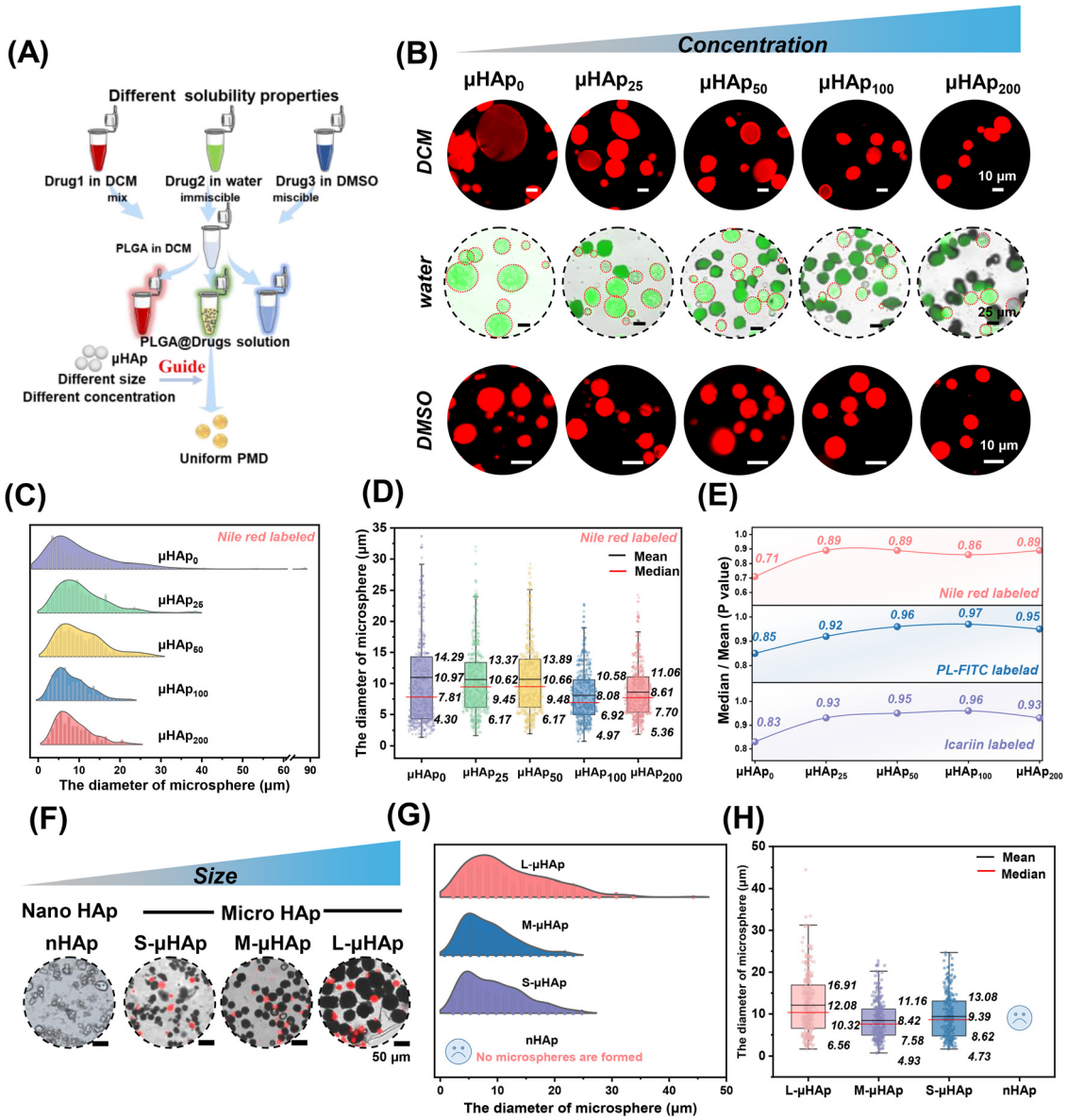

Fig. 2 Formation of uniform PMD by introduction of μHAp. (A) Schematic representation of different solubility drugs in the PMD preparation process. (B) Images of Nile Red labeled, FITC-PL labeled, and Icariin labeled microspheres with different μHAp content, respectively. (C) The kernel density estimation and (D) the box plot of statistical results of Nile red labeled microspheres (the four values are: upper quartile, mean, median, and lower quartile). (E) The ratio of median to mean-P of Nile Red labeled, FITC-PL labeled, and Icariin labeled microspheres with different μHAp content, respectively. (F) The gross view and (G) the kernel density estimation and (H) the box plot of statistical results of labeled microspheres with different sizes of HAp.

the uniformity of PMD, with this improvement positively correlated with HAp content. Since 100 mg mL^{-1} μHAp has already aided the production of more uniform PMD, this content of μHAp was used as a standard for subsequent experiments.

Further, the effect of sizes of HAp on the uniformity of PMD, nano-sized HAp (nHAp) and micro-sized HAp (S-μHAp: 10–25 μm, M-μHAp: 25–40 μm, L-μHAp: 40–70 μm) were investigated with the same concentration of 100 mg mL^{-1}. As shown in Fig. 2H, Nile red labeled PMD was successfully prepared with the introduction of the S-μHAp, M-μHAp and L-μHAp. The uniformity of PMD was best with the guidance of M-μHAp, whereas nHAp resulted in the formation of PLGA debris instead of microspheres (Fig. 2F). Conversely, by reducing the concentration of nHAp to 25 mg mL^{-1}, PLGA microspheres could be obtained (Fig. S4B and C). Previous literature has shown that nHAp can act as an oil–water interfacial stabilizer during the emulsification process based on the Pickering emulsion principle, beneficial for improving the uniformity of microspheres.[41,50,51] However, when the mass concentration of nHAp in the emulsification system is high, excessive nHAp would accumulate on the droplet surface, resulting in the formation of PLGA debris instead of microspheres (Fig. 2F), while its low mass concentration (25 mg mL^{-1}) limits its effectiveness for the biological function of the scaffold. The

results suggest that the sizes of HAp play a significant effect on the uniformity of PMD, nHAp and μHAp promote the formation of uniform PMD through entirely different mechanisms.

Besides, to clarify the mechanism of uniform PMD formation on the existence of μHAp, rheological tests were performed to assess the shear properties of the liquid phase containing different content of μHAp at concentrations of 0, 25, 50, 100 and 200 mg mL^{-1} (Fig. 3A) and different sizes of μHAp (S-μHAp, M-μHAp and L-μHAp) (Fig. 3C). The shear stress increased with content of μHAp and shear rate. Notably, there was an obvious increase in shear stress as the μHAp concentration raised from 50 mg mL^{-1} to 100 mg mL^{-1} (Fig. 3B). Without μHAp, the emulsification process was like a traditional rotor–stator emulsification. To visualize the distribution of shear stress in a rotor–stator emulsification system, we qualitatively and quantitatively demonstrated the shear rate distribution using finite element analysis (Fig. 3D and E). The shear rate in the transverse and longitudinal sections presented the inhomogeneous shear during the emulsification process, explaining the wide distribution of microsphere size observed in the conventional emulsification process or μHAp0. Furthermore, the addition of particle-auxiliary emulsifiers in the emulsification process was beneficial in improving the homogeneity of the shear stress as reported in previous studies.[52,53] In addition, although the uniformity of PMD was best with the existence of M-μHAp compared to S-μHAp and L-μHAp, the shear stress is not significantly higher in the M-μHAp group (Fig. 3C and Fig. S4D). We speculated that larger particles could exert greater collision force on the droplets under the same shear rate, while their lower quantity with the same mass reduces the chance of collision.

Accordingly, a mechanism for solid–liquid interaction between μHAp and CMA/PLGA to trigger rapid emulsification can be proposed: as illustrated in Fig. 3F, in the existence of μHAp, a solid–liquid system is established, oil and aqueous solutions are collectively referred to as liquid phase. The μHAp

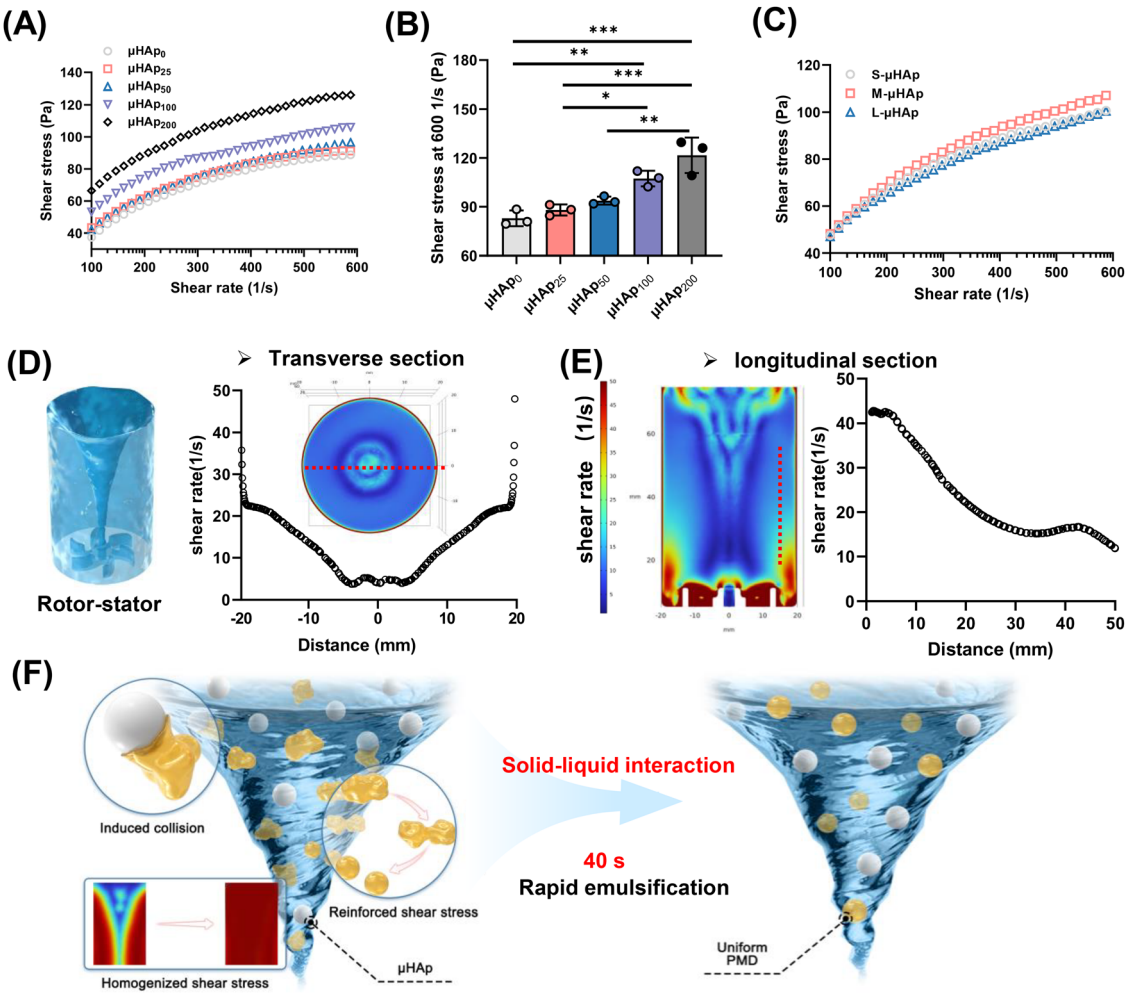

Fig. 3 Mechanism of uniform PMD formation *via* leverage of the solid–liquid interaction between μHAp and CMA/PLGA. (A) Rheological test and (B) quantitative results of shear stress in aqueous solutions with different μHAp content. (C) Rheological test of shear stress in a liquid with different size μHAp. (D) and (E) Finite element analysis and quantitative results of shear rate of a liquid in rotor–stator emulsification in the transverse and longitudinal section (red line). (F) Schematic diagram of the mechanism for solid–liquid interaction between μHAp and CMA/PLGA that triggers emulsification. * $p < 0.05$, ** $P < 0.01$ and *** $P < 0.001$.

in rapid motion collides with the oil droplets, breaking them into smaller droplets, resembling a ''ball milling'' process. Moreover, the μHAp can significantly enhance and homogenize the shear stress of the liquid phase during the vortex. The appropriate size and content of μHAp provides more particles, increasing the collision probability with oil droplets compared to L-μHAp and low concentrations, and offers reinforced shear stress upon collision compared to S-μHAp and low concentrations. As a result, uniform PMD was achieved through the solid–liquid interaction between μHAp and CMA/PLGA triggered by the vortex oscillation in just 40 s.

Release behavior and encapsulation efficiency of drugs in the CHP@Drugs

To demonstrate the versatility of the fabrication of CHP@Drugs *via* leverage solid–liquid interaction, three drugs with different solubilities were chosen: Simvastatin (soluble in DCM), Gentamicin sulfate (soluble in water) and Icariin (soluble in DMSO), as shown in Fig. 4A, E and I, respectively. These drugs can be applied to three kinds of challenging bone repair, corresponding to critical-sized, infected, and osteoporotic bone defects, respectively. The CP@Drugs with non-uniform PMD were used as the control.

Simvastatin (SIM) is a clinical lipid-lowering drug, a common class of drugs with osteogenic activity that promotes bone formation by up-regulating the expression of osteogenesis-related genes and proteins, such as BMP2, at an effective concentration of 5–10 μg mL^{-1}.[54–56] Benefiting from the slow-release effect of PLGA microspheres, CHP@SIM and CP@SIM effectively reduce the abrupt release of the drug (Fig. 4B). Compared to CP@SIM, the cumulative release profiles of the CHP@SIM more closely resemble the optimal monophasic release process, characterized by a stable and constant release rate.[38] Moreover, the real-time concentration of the CHP@SIM group could be maintained within the most effective concentration range (5–10 μg mL^{-1}) for a longer period (Fig. 4C). Besides, the encapsulation efficiency of the drug was determined by collecting microspheres within the scaffold. The results exhibited that uniform microspheres in the CHP@SIM achieved significantly higher drug encapsulation efficiency, approximately 1.36 times greater than that of CP@SIM (Fig. 4D).

Gentamicin sulfate (GEN) is an extensively used water-soluble antibiotic, used in clinic at a safe and effective concentration of about 5–50 μg mL^{-1}.[57] Due to its efficacious antimicrobial properties, it is frequently employed in the management of infected bone defects. However, it is not absorbed from the gastrointestinal tract and is administered exclusively *via* injection or infusion.[58] Systemic administration *via* the intravenous route results in low utilization of the defect site, and local injection administration necessitates more frequent and prolonged treatment cycles. Accordingly, the CHP@GEN was developed for long-term precision delivery. Compared to the CP@GEN group, the CHP@GEN group showed a slower release rate and a more stable release process, maintaining a concentration of around 50 μg mL^{-1} for up to 8 days, accompanied by an encapsulation efficiency that was 1.29 times greater (Fig. 4F and G). In addition, CP@GEN could not reach effective concentrations after only 6 days due to high early release and low encapsulation rates. Nevertheless, due to the intrinsic high hydrophilicity of GEN, GEN easily diffused into the aqueous solutions in the emulsification process, thereby some of the GEN failed to be encapsulated into the PMD, resulting in early leakage at 0–1 days (Fig. 4F) and the relative lower encapsulation efficiency of the CHP@GEN group (Fig. 4H) than that of CHP@SIM.

Icariin (IC) is a widely used drug in the treatment of osteoporotic bone defects and at an effective concentration of 10–20 μM according to our previous study.[17,20] In Fig. 4J, the cumulative release of the CP@IC group (~11.73%) exceeded twice that of CHP@IC (~5.66%) within the first 6 hours. Similar to GEN, CP@IC struggled to reach effective concentrations in later stages due to rapid early release and low encapsulation efficiency (Fig. 4K and L). In contrast, the CHP@IC exhibited reduced early-stage drug release and stabilized real-time concentration within a range of 10–20 μM at subsequent stages.

Furthermore, to clarify the effect of drug adsorption by μHAp on the release behavior, C@Drugs (without μHAp or PMD) and CH@Drugs (without PMD) were investigated. As shown in Fig. S5, the CH@Drugs and C@Drugs exhibited similar release patterns, with CH@Drugs not significantly slowing the release rate of drugs compared to C@Drugs. In addition, since there was no PMD in the CH@Drugs and C@Drugs groups, a burst release of drugs from the scaffolds occurred within 1 day, with the cumulative release of SIM and IC exceeding 60%, and GEN approaching 90%. The results demonstrate that μHAp itself in the scaffold had little effect on sustaining drugs and further confirmed that the scaffolds with PMD significantly inhibited the burst release compared to directly loading drugs into the scaffold, which is consistent with previous studies.[29,59]

In short, the results demonstrate that the uniform PMD in CHP@Drugs manipulates the encapsulation and release profiles of the drugs, as shown in Fig. 4M. Previous research has shown that microspheres of varying sizes exhibit significant differences in drug encapsulation efficiency, with larger microspheres generally demonstrating higher encapsulation rates.[60] The frequency distribution histogram (Fig. S6) indicates that the PMD in the CP@Drugs exhibits a broader dispersion, featuring a greater number of smaller and larger PMD compared to CHP@Drugs. Thus, a reduction in the encapsulation efficiency in the CP@Drugs is owing to the presence of a greater number of smaller PMD. Conversely, the CHP@Drugs exhibited relatively high encapsulation rates, attributed to the uniform and moderate size of PMD. In addition, the uniformity and size of microspheres are also important factors that affect the drug release process.[38,39,61] Smaller sized PMD typically have a relatively shorter drug release pathway, allowing for more drug release from the microspheres, whereas larger PMDs create longer pathways, hindering sustained release.[39] In contrast, the drug release rate from uniform PMD was stable and slower in the early stages compared to the PMD of the same average size but with a wider distribution.[62] Our results indicate that the CP@Drugs group initially released a significant amount of drug and later struggled to maintain effective concentration. In contrast, the CHP@Drugs exhibited a more optimal release profile, characterized by maintaining a stable, safe, and

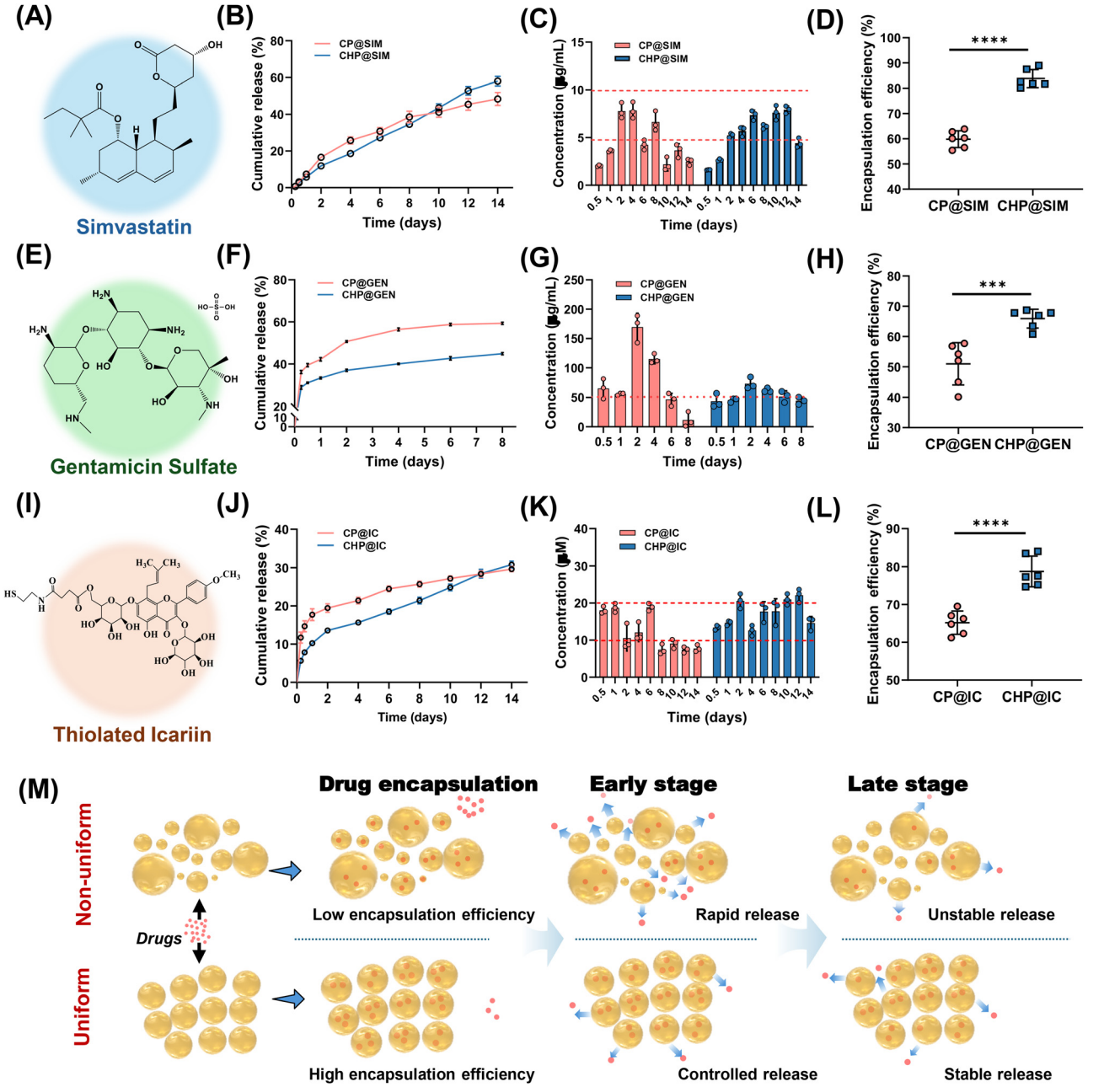

Fig. 4 The encapsulation efficiency and release behavior of three different solubility properties of drugs loaded in CHP@Drugs and CP@Drugs respectively. (A), (E) and (I) The structural formula of three representative drugs (SIM, GEN and IC) with varying solubility properties for bone repair. (B) Cumulative release, (C) real-time concentration and (D) the encapsulation efficiency of drugs in the CP@SIM and CHP@SIM. (F) Cumulative release, (G) real-time concentration, and (H) the encapsulation efficiency of drugs in the CP@GEN and CHP@GEN. (J) Cumulative release, (K) real-time concentration, and (L) the encapsulation efficiency of drugs in the CP@IC and CHP@IC. (M) Schematic diagram of drug encapsulation and release of uniform and non-uniform PMD. ***$P < 0.001$, ****$P < 0.0001$.

effective concentration range for sustained release throughout both early and later stages. These results suggest that PMD effectively controlled the drug release, and uniform PMD enhanced the stability and sustainability of the release process.

CHP@Drugs for the treatment of challenging bone defects

To evaluate the effectiveness of CHP@Drugs loaded with different drugs (SIM, GEN, and IC) in treating challenging bone defects, three rat bone defect models were established: a critical-sized cranial defect, an infected cranial defect, and an osteoporotic femur defect (Fig. 5A, 6A and 7A, respectively). Maintaining real-time concentrations within a safe range for the CHP@Drugs is a prerequisite for effective treatment.[63] Thus, the initial compatibility and spread of BMSCs on the CHP@Drugs were first assessed before investigating the scaffolds' potential for bone repair. As shown in Fig. 5B, 6B, 7B and

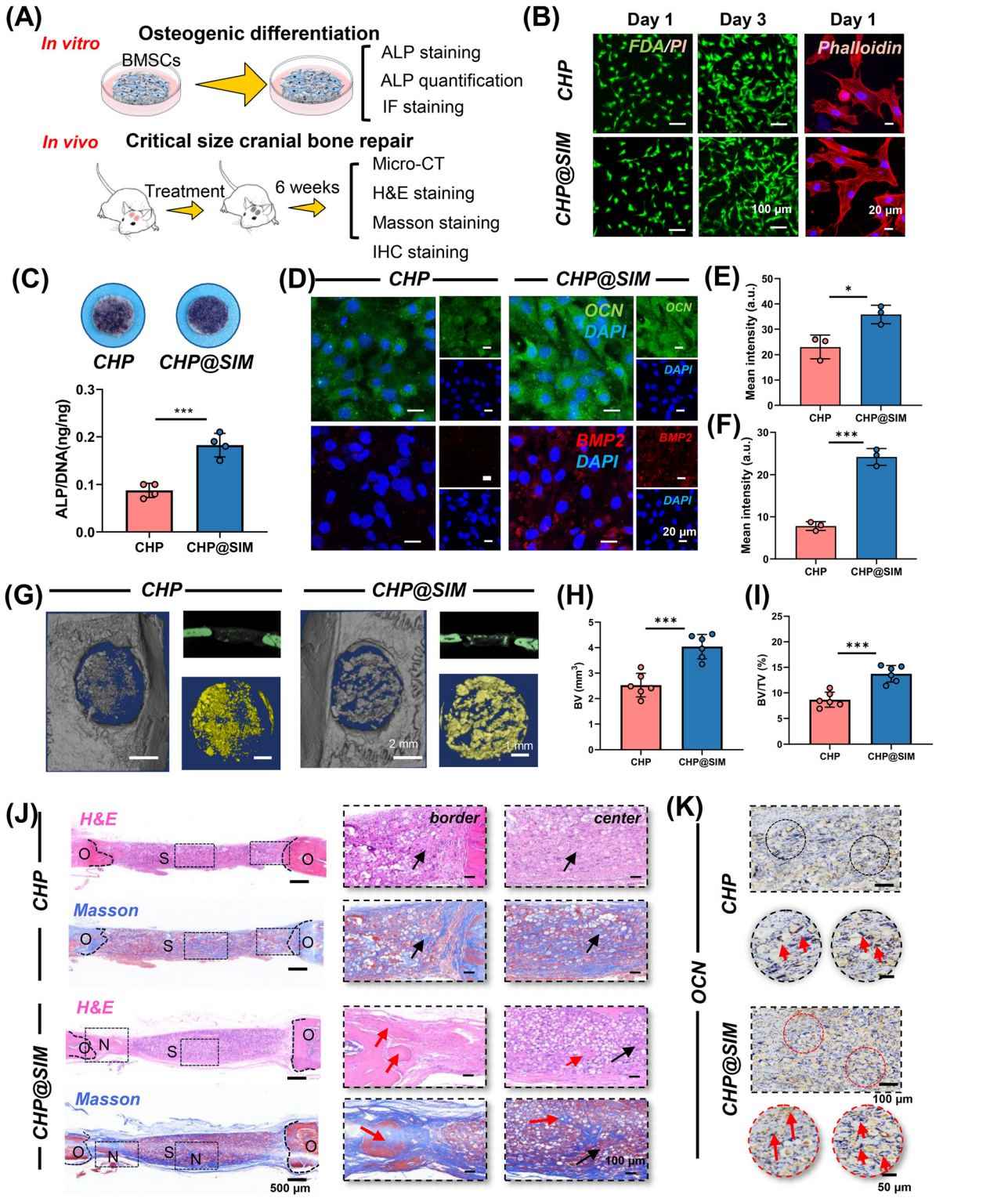

Fig. 5 The CHP@SIM for repair of critical-sized cranial defects in rats. (A) Experimental procedures *in vitro* and *in vivo*. (B) The live/dead and F-actin staining of BMSCs co-cultured with the CHP@SIM and CHP. (C) The ALP staining and quantitative analysis of the ALP secretion (n = 4). (D) Images, (E) and (F) quantification of mean fluorescence intensity of OCN and BMP2 treated by CHP and CHP@SIM *in vitro* (n = 3). (G) Micro-CT analysis of cranial bone defects after 6 weeks of treatment. (H) Bone volume and (I) bone volume normalized to total tissue volume (BV/TV) in the cranial defects after 6 weeks of treatment (n = 6). (J) H&E and Masson trichrome staining of the defects after 6 weeks (O: old bone, N: new bone, S: scaffold, red arrow: new bone and black arrow: immature bone matrix). (K) Immunohistochemical staining of OCN of the defects after 6 weeks (red arrow: OCN positive cells). *P < 0.05 and ***P < 0.001.

Fig. S7, the BMSCs spread well and gradually proliferated over time, displaying a consistent proliferation trend with no significant difference among all groups. These results indicate that all CHP@Drugs have good biocompatibility, and the drug concentrations released from each CHP@Drugs remained within a safe range. Subsequently, the effectiveness of

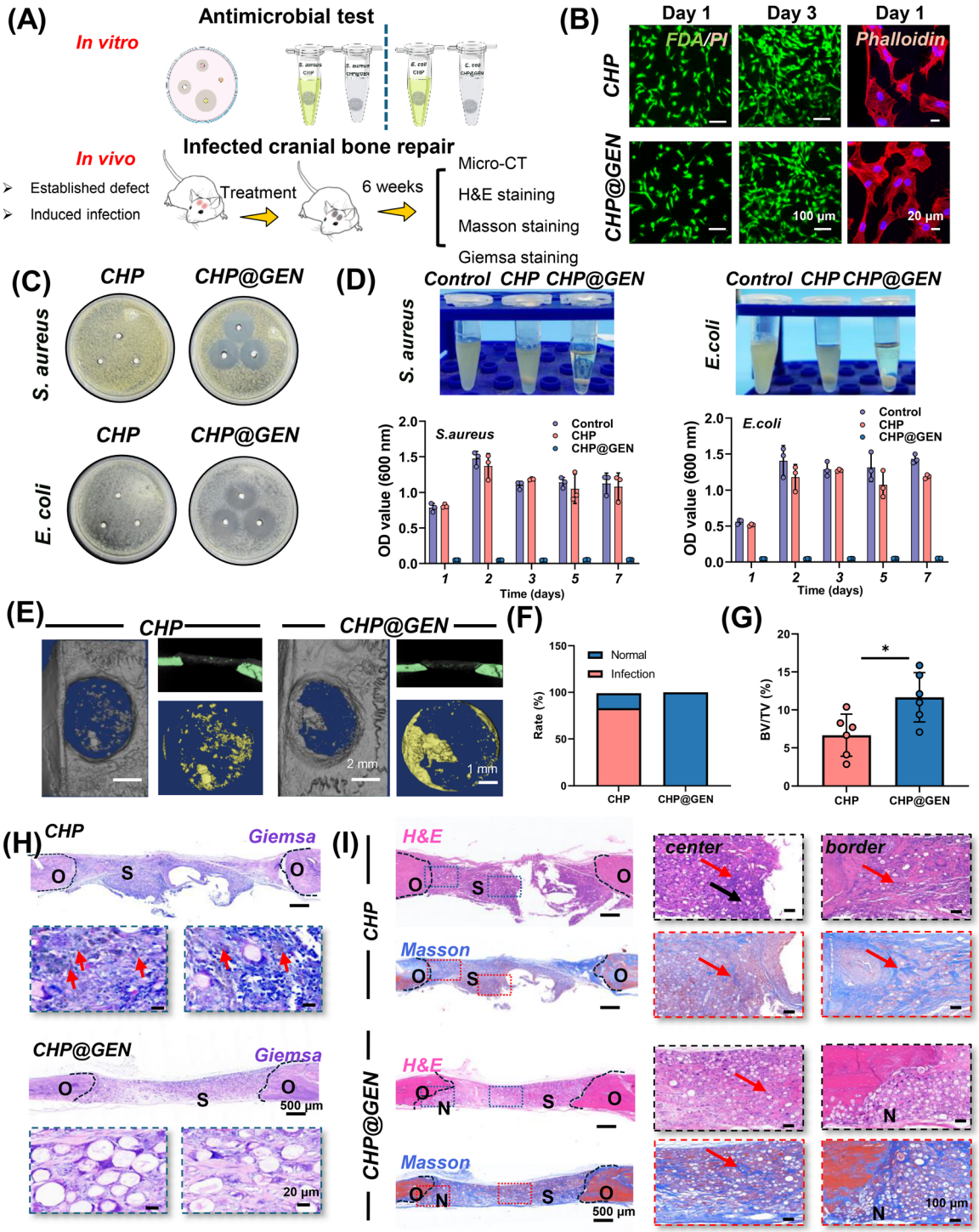

Fig. 6 The CHP@GEN for repair of infected cranial defects. (A) Experimental procedures *in vitro* and *in vivo*. (B) The live/dead and F-actin staining of BMSCs co-cultured with the CHP@GEN and CHP. (C) The inhibited zone against both *S. aureus* and *E. coli* treated by CHP and CHP@GEN (n = 3). (D) The images and turbidity values of the *S. aureus* and *E. coli* co-cultured with CHP and CHP@GEN for a 7-day acute infected period (n = 3). (E) Micro-CT 3D-reconstruction images, (F) infected rate analysis (n = 6) and (G) quantitative analysis of BV/TV (n = 6) for infected cranial defects after 6 weeks of treatment. (H) Giemsa staining (red arrow: bacteria) and (I) H&E and Masson trichrome staining (O: old bone, N: new bone, S: scaffold, red arrow: immature bone matrix and black arrow: inflammatory cell) of the infected bone defects after 6 weeks of treatment. *$P < 0.05$.

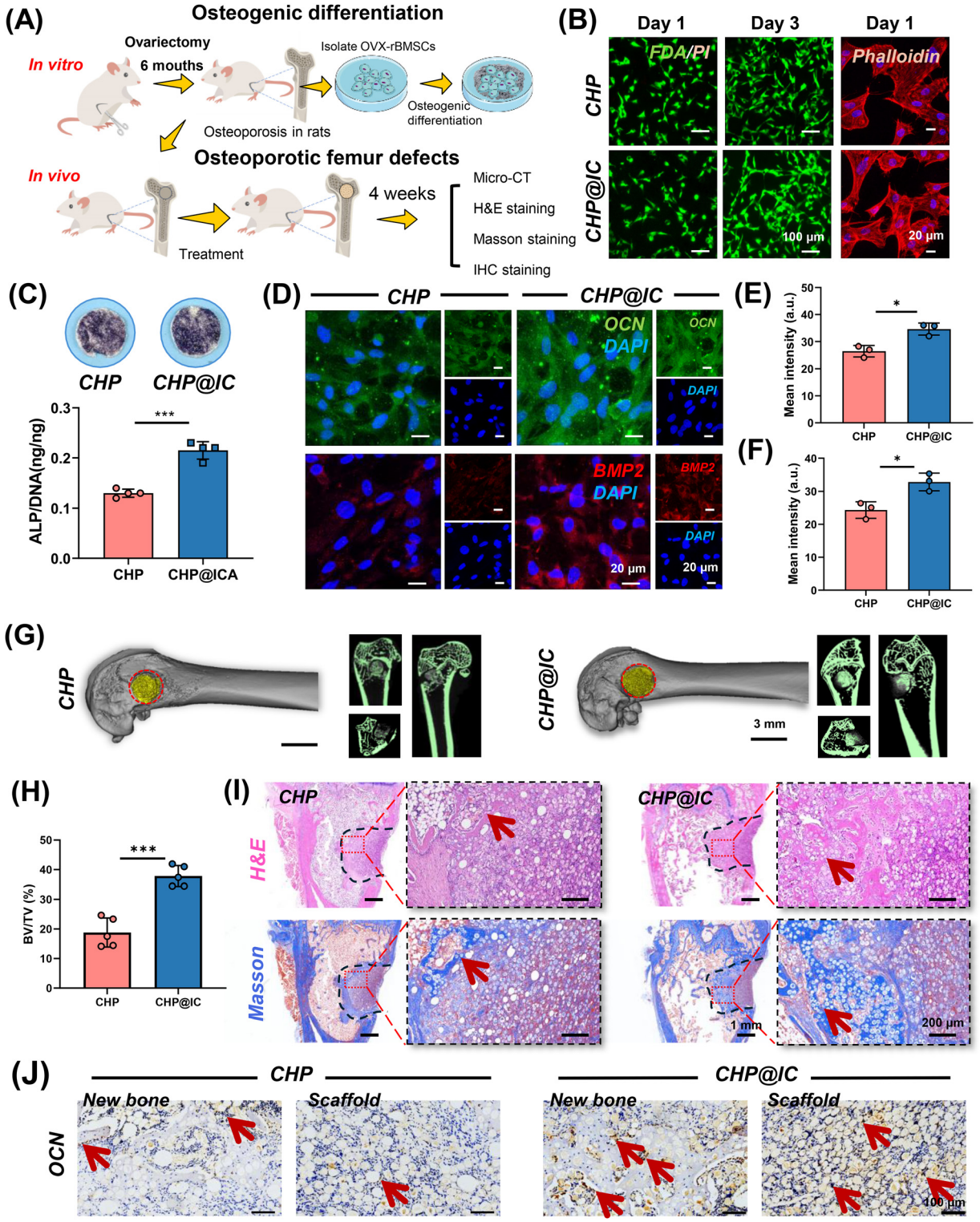

Fig. 7 The CHP@IC for repair of osteoporotic femur defects. (A) Experimental procedures *in vitro* and *in vivo*. (B) The live/dead and F-actin staining of BMSCs co-cultured with the CHP@IC and CHP. (C) The ALP staining and ALP activity (n = 4), (D) immunofluorescence staining of OCN and BMP2 (E) and (F) quantification of mean fluorescence intensity of OCN and BMP2 (n = 3) of OVX-BMSCs treated by CHP and CHP@IC after 7 days. (G) Micro-CT 3D-reconstruction images, (H) quantitative analysis of BV/TV (n = 5), (I) H&E and Masson trichrome staining (red arrow: new bone), (J) immunohistochemical staining of OCN (red arrow: OCN positive cells) for osteoporotic femur defects after 4 weeks of treatment by CHP and CHP@IC. $^{*}P < 0.05$ and $^{***}P < 0.001$.

CHP@Drugs was investigated both *in vitro* and *in vivo*, and the CHP without drugs was the control group.

CHP@SIM for the repair of critical-sized cranial defects

CHP@SIM was applied to repair critical-sized cranial defects. The effect of the CHP@SIM on osteogenic differentiation of BMSC *in vitro* was first investigated. After 7 days of co-culture, the ALP staining and quantitative analysis showed that the CHP@SIM significantly promoted higher ALP expression in BMSCs compared to the CHP (Fig. 5C). Immunofluorescent staining for BMP2 and OCN (Fig. 5D–F) further suggested that the CHP@SIM enhanced the secretion of osteogenic-related proteins in BMSCs during early osteogenic differentiation. The results demonstrate that CHP@SIM could effectively facilitate the osteogenic differentiation of BMSCs *in vitro*. CHP@SIM was then implanted into the rats' critical-sized cranial defects. After 6 weeks of treatment, the Micro-CT reconstructed images exhibited that the CHP@SIM led to more new bone formation at the defect sites (Fig. 5G), with the bone volume to total volume (BV/TV) ratio increased by 50% compared to the CHP (Fig. 5H). Furthermore, H&E staining showed that the cells fully infiltrated into both the CHP and CHP@SIM in Fig. 5J. A comparative analysis of H&E and Masson's trichrome staining was conducted between the edge of the scaffolds in contact with the bone and the central part of the scaffolds. The results indicated that the peripheral regions of the CHP@SIM exhibited new and more mature bone tissue growth, along with substantial bone matrix formation in the center of the scaffold. In contrast, only a small amount of bone matrix was observed in the CHP group. In addition, immunohistochemical staining (Fig. 5K) further displayed a large amount of OCN positive staining in the CHP@SIM group. These results demonstrate that CHP@SIM accelerated repair of critical-sized cranial defects in rats.

CHP@GEN for the repair of infected cranial defects

The regeneration of infected bone defects is a significant global challenge. To effectively treat infected defects, continuous vigilance against bacterial infections is crucial, as infection can impede the optimal treatment window and potentially lead to severe conditions like osteomyelitis or even amputation.[64] It is imperative to develop a stable, localized antibiotic delivery strategy that provides prolonged treatment of the infected site and simultaneously facilitates repair of the bone defect. As shown in Fig. 6A, CHP@GEN is expected to repair infected bone defects. First, the antimicrobial capacity of CHP@GEN was assessed *in vitro*. Compared to the CHP, the CHP@GEN formed larger inhibition zones against both Gram-positive (*S. aureus*) and Gram-negative (*E. coli*) bacteria, demonstrating enhanced antimicrobial capacity (Fig. 6C). To further assess whether the GEN released from CHP@GEN could provide sustained and long-term bacterial inhibition, the scaffolds were co-cultured with *S. aureus* and *E. coli* for a 7-day acute infection period. As shown by the turbidity values and general photographs in Fig. 6D, the turbidity levels observed in the CHP group were comparable to the pure bacterial culture, indicating no antibacterial effect during the 7-day co-culture period. In contrast, CHP@GEN completely inhibited the growth of the bacteria over 7 days, resulting in a clarified co-cultured solution. The results suggest that the stabilized release of GEN from the scaffold maintains an effective antimicrobial concentration, significantly reducing the risk of infection.

Subsequently, the CHP@GEN was implanted into the infected cranial defect models induced by high concentrations of *S. aureus*. After 6 weeks of treatment, the CHP group showed a high infection rate of 83.33% in all the animal samples (Fig. 6F), with minimal new bone formation in the post-infected defects (Fig. 6E and G). Additionally, the CHP group also exhibited destructive degradation and substantial infiltration of inflammatory cells, as well as a large number of bacteria in the defects (Fig. 6H and I). In contrast, the CHP@GEN was in line with the normal process of bone defect repair, with substantial infiltration regeneration-related cells secreting extracellular matrix and new bone growth observed at the scaffold's edges. Notably, no evident bacterial infection was detected in the defects treated with CHP@GEN (Fig. 6F, H and I). These results demonstrate that the CHP@GEN effectively prevents or treats bacterial infection during bone defect repair by delivering GEN, thereby providing a stable and safe regenerative environment for subsequent bone healing.

CHP@IC for the repair of osteoporotic femur defects

The regeneration of osteoporotic bone defects is hindered by disrupted homeostasis, resulting in a prolonged bone repair process. As shown in Fig. 7A, CHP@IC was applied to repair osteoporotic femur defects. The osteogenic differentiation of OVX-BMSCs from the osteoporotic rats was assessed *in vitro* using CHP@IC. The ALP staining and quantitative analysis showed that CHP@IC significantly promoted higher ALP expression in OVX-BMSCs (Fig. 7C). Immunofluorescent staining for BMP2 and OCN (Fig. 7D and F) further demonstrated that the CHP@IC enhanced the secretion of osteogenic-related proteins in OVX-BMSCs during early osteogenic differentiation, thereby promoting their osteogenic differentiation. Subsequently, the CHP@IC was implanted into metaphyseal defects in osteoporotic rat femurs. After 4 weeks of treatment, micro-CT 3D reconstruction images showed that the CHP@IC group significantly promoted the new bone formation, and quantitative data of BV/TV revealed that the CHP@IC group ($\sim$37.86%) had a twofold increase compared to the control group (18.81%) (Fig. 7G and H). The H&E staining (Fig. 7I) demonstrated that a large number of cells infiltrated into both the CHP@IC and the CHP groups. In addition, the amount of new bone in the CHP group was minimal, with a considerable amount of fibrous tissue surrounding the scaffold. In contrast, the CHP@IC group exhibited a notable increase in new bone formation within the scaffold. Masson's trichrome staining showed an enhanced red margin in the new bone formed by CHP@IC, suggesting a higher degree of bone maturation (Fig. 7I). And dense new bone tissue and bone trabecular structures were also observed in the magnified images. Immunohistochemical staining of the osteogenesis-related protein OCN was more positive expression

in the CHP@IC (Fig. 7J), further demonstrating bone-promoting activity of the CHP@IC.

Conclusions

In this study, we present a facile method to fabricate CHP@Drugs in a continuous, rapid, and time-saving process, breaking through the limitation of the traditional "first preparation – then encapsulation" method. Moreover, CHP@Drugs were flexibly designed for the repair of challenging bone defects. Notably, owing to the induced collision where the shear stress was homogenized and reinforced from the solid–liquid interaction between μHAp and CMA/PLGA triggered by vortex oscillation in just 40 s, the uniform PMD in site preparation and simultaneous encapsulation within CHP@Drugs was achieved, resulting in stable and sustained drug release of CHP@Drug. In addition, the CHP@Drugs with FDA-approved components, exhibited an interconnected porous structure and strong potential for clinical application in repairing challenging bone defects.

The proposed mechanism for solid–liquid interaction between μHAp and CMA/PLGA, enabling in site preparation and simultaneous encapsulation of drug-loaded microspheres rapidly and uniformly, has the potential to be developed into a universal approach. By substituting different solid-phase micro-sized particles (*e.g.*, bioactive glass, functional particles, *etc.*) and aqueous solutions (*e.g.*, methacrylate modified hyaluronic acid, chitosan or gelatin, *etc.*), this strategy can be extended to construct drug delivery platforms and scaffolds for the repair of other tissues, such as skin, muscle, nerve, *etc.* Nonetheless, it is still in its infancy and some challenges should be further investigated to widen the range of its applications. First, the CHP@Drugs can be designed to deliver two or more drugs simultaneously to address more complex pathological environments. Second, every effort needs to be made to overcome the challenge of analysing the shear rate distribution in this solid–liquid system using finite element analysis in future studies. In addition, multiple concentration gradients need to be designed for the delivery system to determine the optimal release pattern and effective concentration for fulfilling the desired biological function, necessitating more in-depth and longer-term investigations.

Together, this study advances the design approach of scaffolds for challenging bone repair and overcomes the complicated and time-consuming preparation of the drug-microsphere encapsulated bone-repair scaffold, offering a facile, rapid, and efficient fabrication of CHP@Drugs for the enhanced repair of challenging bone defects, and a universal approach to fabricate drug-microsphere encapsulated scaffolds for other tissue repair.

Experimental

Preparation of CHP@Drugs

Drugs dissolved in 30 μL DCM, water, and DMSO were separately added to 100 μL PLGA solution to obtain three distinct oil solutions: drug dissolved in PLGA solution, drug–PLGA immiscible solution and drug–PLGA miscible solution. Each oil solution was then gradually added dropwise to a CMA/μHAp solution containing a photo-initiator under agitation on a vortex oscillator. After 40 s of emulsification, the resulting emulsion was rapidly solidified by exposure to 405 nm light for 90 s, forming the CHP@Drugs hydrogel in site. The final concentrations of CMA, photo-initiator and PLGA were 10 mg mL^{-1}, 0.6 mg mL^{-1} and 6 mg mL^{-1}, respectively. Subsequently, the CHP@Drugs hydrogel was lyophilized for 1 day. A series of CHP@Drugs were respectively fabricated with varying μHAp content (0, 25, 50, 100 and 200 mg mL^{-1}). For comparison, the CH@Drugs were prepared by directly adding the drug solution to the CMA/μHAp mixture solution. In addition, the CP@Drugs were fabricated by adding the oil phase to the CMA solution in the absence of μHAp, and the CHP was produced without loading drugs.

Characterization of scaffolds

The surface and internal morphology of scaffolds were examined using a stereomicroscope (SteREO Discovery.V20, Zeiss), a 3D Optical Profiler (Sensofar S NEOX 90), and scanning electron microscopy (Hitachi, Japan). The mechanical properties of the scaffolds, post-swelling equilibrium, were measured by a dynamic mechanical analyzer (DMA, TA-Q800, USA) with a preload force of 0.01 N, and a ramp force of 0.1 N min^{-1} up to 2 N.

The water absorption ratio of scaffolds was determined based on gravimetric measurements. The initial weight of the lyophilized scaffold (W_0) was recorded, followed by soaking in Tris–HCl buffer solution (pH = 7.4). The wet weight of the scaffold (W_w) was measured at pre-set time points, and the water absorption ratio was calculated using the formula: water absorption ratio (%) = $(W_w - W_0)/W_0 \times 100\%$.

Characterization of PMD

To simulate and visualize the encapsulation process, three types of fluorescent molecules – Nile red, PL-FITC and Icariin – were incorporated to the oil-phase solution. Microsphere visualization was performed using fluorescence microscopy (Zeiss, Germany) after enzymatic degradation of the scaffolds with collagenase I (Solarbio, China), to facilitate observation. Then, the size distribution of the microspheres containing Nile red (n = 600), PL-FITC (n = 300) and Icariin (n = 600) were analyzed using Image J software.

Preparation of representative CHP@Drugs

Firstly, simvastatin (500 μg), gentamicin sulfate (12.5 mg) and thiolated icariin (3 mg) were respectively dissolved in 30 μL of DCM, water and DMSO, and then combined with 100 μL of 60 mg mL^{-1} of PLGA solution. The resulting solutions were designated as oil 1, 2 and 3, respectively. Each oil solution was then individually introduced dropwise into the CMA/HAp solution following the established CHP@Drugs preparation method, yielding CHP@SIM, CHP@GEN and CHP@IC. Additionally, the same oil solutions were introduced into CMA

solutions without μHAp, producing non-uniform PMD-encapsulated scaffolds, named CP@SIM, CP@GEN and CP@IC. Furthermore, the above three drugs were directly added into CMA and CMA/HAp solutions to prepare additional scaffolds, designated as C@SIM, C@GEN, C@IC, CH@SIM, CH@GEN and CH@IC, respectively.

Drug release behaviour of scaffolds

The above scaffolds (φ = 12 mm, h = 1.5 mm) were submerged in 1 mL of Tris–HCl solution. At the designated time point, the solution was fully collected and subjected to centrifugation. The supernatants were subsequently analyzed using an ultraviolet spectrophotometer (UV-vis, Thermo Scientific, USA). Among them, the characteristic UV-vis absorption peaks of simvastatin (247 nm) and thiolated icariin (360 nm) were used to quantify the drug content in the supernatants accurately.[17,55] The gentamicin sulfate content was determined using a derivatization method, with an ultraviolet absorption peak at 330 nm (Fig. S8).[57] Based on the above methods, the cumulative drug release was calculated using the formula: cumulative release (%) = $W_t/W \times 100\%$, where W and W_t represent the total drug content and the released drug content, respectively.

Encapsulation efficiency of scaffolds

To determine the encapsulation efficiency of various drugs within the PLGA microspheres in each scaffold, the scaffolds were completely degraded with collagenase I (0.1 mg mL^{-1}) at 37 °C. The resulting precipitates were collected, dissolved in DMSO, and analyzed using an ultraviolet spectrophotometer. The encapsulation efficiency was calculated using the following formula: encapsulation efficiency (%) = $W_e/W \times 100\%$, where W and W_e represent the total drug content and the drug content encapsulated in PLGA microspheres, respectively.

Finite element and rheological analysis

A stator–rotor model, constructed within the Comsol6.1 (USA) was employed to simulate the rotor–stator emulsification process within a vessel with a radius of 4 cm and a height of 6 cm. The shear rate distribution during emulsification at a stirring rate of 600 1 s^{-1} was analyzed, and the quantitative data was obtained. The rheological properties of CMA containing different contents and sizes of HAp were investigated using a rheometer MCR302 (Anton Paar, Austria). Shear stress variations were measured across a shear rate range from 100 to 600 s^{-1}.

Cytocompatibility of the scaffolds

Bone marrow mesenchymal stem cells (BMSCs, 1×10^4 cells) were initially seeded on sterilized scaffolds. The culture medium consisted of α-MEM (Corning, USA) supplemented with 10% FBS (Gibco, USA) and 1% penicillin–streptomycin (Gibco, USA). The cells were then incubated at 37 °C in a 5% CO_2 atmosphere for 1 and 3 days. Cell proliferation was evaluated using the Cell Counting Kit-8 (CCK-8) assay (Solarbio, China) at 450 nm. Fluorescein diacetate (Sigma-Aldric, USA) and propidium iodide (Sigma-Aldric, USA) were employed for the staining of live (green) and dead (red) cells, respectively, while F-actin and DAPI (Solarbio, China) were utilized for visualizing cytoskeleton and cell nucleus, respectively.

ALP expression *in vitro*

BMSCs and BMSCs isolated from ovariectomy rats (OVX-rBMSCs) (5×10^4 cells) were cultured on CHP, CHP@SIM and CHP@IC for 7 days. On day 7, cells were lysed using RIPA lysis buffer (Solarbio, China), and the supernatants were collected to detect ALP expression using a pNPP Alkaline Phosphatase Assay Kit (SensoLyte, USA). The total DNA content was quantified with a Picogreen™ dye-based fluorescent DNA Quantification Kit (Invitrogen, USA) for normalization of ALP activity. The ALP staining was conducted using a BCIP/NBT ALP staining kit (Beyotime, China).

Immunofluorescence staining *in vitro*

Additionally, osteogenesis-related proteins BMP2 and OCN expression in cells was observed through immunofluorescence staining. Primary antibodies against BMP2 (1 : 100 dilution, Ab284387, Abcam, UK) and OCN (1 : 100 dilution, 23418-1-AP, Proteintech, UK) were applied respectively, followed by secondary antibodies in a sequential manner. The cell nuclei were counterstained with DAPI (Solarbio, China). The protein expression in cells was then visualized using a confocal laser scanning microscope (CLSM, Zeiss, Germany), and the optical density was quantified with Image J software.

Antibacterial experiment

Antimicrobial properties were evaluated using turbidimetric methods and zone of inhibition assays. Scaffolds (CHP@GEN and CHP) were co-cultured with a bacterial suspension (600 μL of 10^6 CFU per mL, *S. aureus* and *E. coli*). At the designated time points, 200 μL of the culture supernatant was collected, and the optical density was determined at 600 nm. To assess the long-term bacteriostatic efficacy, 200 μL of fresh LB bacterial medium was added for continued cultivation. For the zone of inhibition assay, 50 μL of 10^5 CFU per mL bacterial suspension was evenly spread on the LB solid agar plate. Then, the scaffolds were placed on the agar plates, and 20 μL of Tris–HCL solution was added to each scaffold to facilitate drug release. After 12 hours of culture, the inhibition zones were photographed with a digital camera.

Animal experiment

All animal experiments in this literature were approved by the animal ethics committee of Sichuan University (Approval No. KS2021698).

Subcutaneous implantation. To evaluate the differences in tissue infiltration of scaffolds, CH@Drug and CHP@Drug (φ = 5 mm, h = 1.5 mm) were implanted into the subcutaneous pockets at the back of five eight-week-old male rats. After 7 days, scaffolds were collected to assess tissue infiltration in scaffolds.

Cranial defect and infected cranial defect models. Twenty 8-week-old male rats were randomly divided into two groups.

After the rats were anesthetized, a full-thickness cranial defect with a critical size of 5 mm was constructed on both sides of the skull using a dental drill. For one group, the sterilized scaffold (CHP and CHP@SIM) was implanted into the defect sites. In the second group, defects were infected with 50 μL of 10^8 CFU per mL bacterial suspension and treated with CHP and CHP@GEN. After a six-week course of treatment, the skulls of two groups were harvested and fixed in 4% paraformaldehyde for two days.

Osteoporotic rat bone defect mode. 8-Week-old female rats were anesthetized and underwent ovariectomy to induce osteoporosis.[20] After 24 weeks, the OVX-rat model was used for bilateral femoral condylar defect surgery. Briefly, after OVX-rats were anesthetized, the skin and muscle of the distal femur were bluntly separated to expose the femoral condyles, and a columnar defect (φ = 3 mm, h = 3 mm) was created with a dental drill under saline irrigation, and CHP and CHP@IC were alternately implanted in the right or left femoral defects of rats. Then, the muscle and skin were sutured after implantation. Four weeks after implantation, the femurs of the rats were harvested.

Micro-CT analysis

All defects of the above groups were scanned topographically using a Quantum GX micro-CT imaging system (PerkinElmer, USA) at a scanning accuracy of 15 μm, and the data were completely reconstructed and analyzed with Mimics software (Materialise, Belgium).

Histological and immunohistochemistry staining

All the samples of animal experiment were decalcified in 10% EDTA solution for 4 weeks, then embedded in paraffin and sectioned into 5-μm-thickness slices. Histological staining was performed according to H&E, Giemsa and Masson trichrome staining kits (Solarbio, China).

For the immunohistochemistry staining, sections were subjected to antigen retrieval, endogenous catalase, and blocking with 10% goat serum. Primary (1 : 100, dilution 23418-1-AP, Proteintech, UK) and secondary antibodies targeting osteogenic protein OCN were applied, followed by visualization using a DAB kit (Solarbio, China).

Statistical analysis

All the experiments were repeated at least three times, and all obtained data were presented as mean ± standard deviation. Statistical analysis was performed using a t-test, or one-way ANOVA in GraphPad Prism 8.0. Statistically significant values were indicated as $^*P < 0.05$, $^{**}P < 0.01$, $^{***}P < 0.001$ and $^{****}P < 0.0001$.

Author contributions

Fengxin Zhao: investigation, validation, writing – original draft. Puxin Liu: investigation, conceptualization, software. Xinyi Wang: methodology. Jirong Yang: methodology, funding acquisition, writing – review and editing. Changshun Ruan: writing – review and editing, supervision. Dongxiao Li: supervision. Xiangdong Zhu: supervision. Yumei Xiao: conceptualization, funding acquisition, supervision, writing – review and editing. Xingdong Zhang: supervision.

Conflicts of interest

There are no conflicts to declare.

Abbreviations

CMA	Methacrylate anhydride-modified collagen
μHAp	Micro-hydroxyapatite
PLGA	Poly(lactic-*co*-glycolic acid)
Oil solution	PLGA solution or PLGA solution contained drugs
Aqueous solution	CMA solution
PMD	Drug-loaded PLGA microspheres
Liquid phase	CMA mix with PLGA solution
Solid phase	Micro-hydroxyapatite
CHP@Drugs	CMA/HAp/PLGA/Drugs scaffold
CP@Drugs	CMA/PLGA/Drugs scaffold
CH@Drugs	CMA/HAp/Drugs scaffold
C@Drugs	CMA/Drugs scaffold
SIM	Simvastatin
GEN	Gentamicin sulfate
IC	Icariin

Data availability

All data that support the results of this study are available from the corresponding author upon reasonable request.

Supplementary information (SI) is available. See DOI: https://doi.org/10.1039/d5mh01359c.

Acknowledgements

This study is supported by the Sichuan Science and Technology Program for Regional Innovation Cooperation (2024YFHZ0184), the Shenzhen Medical Research Fund (No. A2303016, B2402016), the National Natural Science Foundation of China (Grant No. 92468106), and the Shenzhen Fundamental Research Foundation (JCYJ20240813154723030). The authors thank Yanfei Tan, Jiao Lv, Guolong Meng and Lingzhu Yu for their help with SEM, CLSM and other measurements.

References

1 G. L. Koons, M. Diba and A. G. Mikos, *Nat. Rev. Mater.*, 2020, **5**, 584–603.
2 D. Tang, R. S. Tare, L.-Y. Yang, D. F. Williams, K.-L. Ou and R. O. C. Oreffo, *Biomaterials*, 2016, **83**, 363–382.
3 A. Ho-Shui-Ling, J. Bolander, L. E. Rustom, A. W. Johnson, F. P. Luyten and C. Picart, *Biomaterials*, 2018, **180**, 143–162.

4 J. Yang, Z. Chen, C. Gao, J. Liu, K. Liu, X. Wang, X. Pan, G. Wang, H. Sang, H. Pan, W. Liu and C. Ruan, *Nat. Commun.*, 2024, **15**, 3565.
5 Y. Fan, H. Ran, Z. Wang, C. Ning, J. Zhai and P. Yu, *Adv. Funct. Mater.*, 2024, **34**, 2308310.
6 M. Li, Y. Fan, M. Ran, H. Chen, J. Han, J. Zhai, Z. Wang, C. Ning, Z. Shi and P. Yu, *Adv. Healthcare Mater.*, 2024, **13**, 2401296.
7 D. Aggarwal, V. Kumar and S. Sharma, *J. Controlled Release*, 2022, **344**, 113–133.
8 M. Janmohammadi, Z. Nazemi, A. O. M. Salehi, A. Seyfoori, J. V. John, M. S. Nourbakhsh and M. Akbari, *Bioact. Mater.*, 2023, **20**, 137–163.
9 A. Zielińska, J. Karczewski, P. Eder, T. Kolanowski, M. Szalata, K. Wielgus, M. Szalata, D. Kim, S. R. Shin, R. Słomski and E. B. Souto, *J. Controlled Release*, 2023, **359**, 207–223.
10 Y. Zeng, J. Hoque and S. Varghese, *Acta Biomater.*, 2019, **93**, 152–168.
11 U. G. K. Wegst, H. Bai, E. Saiz, A. P. Tomsia and R. O. Ritchie, *Nat. Mater.*, 2014, **14**, 23–36.
12 S. S. Lee, N. Kleger, G. A. Kuhn, H. Greutert, X. Du, T. Smit, A. R. Studart and S. J. Ferguson, *Adv. Mater.*, 2023, **35**, 2302008.
13 E. A. Guzzi, G. Bovone and M. W. Tibbitt, *Small*, 2019, **15**, 1905421.
14 W. Dang, K. Yi, E. Ju, Y. Jin, Y. Xu, H. Wang, W.-C. Chen, K. Wang, Y. Wang, Y. Tao and M. Li, *ACS Appl. Mater. Interfaces*, 2021, **13**, 18488–18499.
15 H. Uludag, D. D'Augusta, R. Palmer, G. Timony and J. Wozney, *J. Biomed. Mater. Res.*, 1999, **46**, 193–202.
16 J. Chen, J. Luo, J. Feng, Y. Wang, H. Lv and Y. Zhou, *J. Controlled Release*, 2024, **372**, 846–861.
17 Z. Luo, X. Chen, M. Liu, Y. Wang, D. Li, X. Li, Y. Xiao, Y. Wang and X. Zhang, *Mater. Des.*, 2021, **200**, 109468.
18 Y. Chen, W. Liu, S. Wan, H. Wang, Y. Chen, H. Zhao, C. Zhang, K. Liu, T. Zhou, L. Jiang, Q. Cheng and X. Deng, *Adv. Funct. Mater.*, 2023, **34**, 2309191.
19 J. Kost, E. Mathiowitz and A. Azagury, *Adv. Funct. Mater.*, 2021, **31**, 2108838.
20 T. Song, J. Yang, P. Liu, M. Liu, D. Li, Y. Xiao, Y. Wang and X. Zhang, *Composites, Part B*, 2022, **235**, 109759.
21 T.-M. De Witte, L. E. Fratila-Apachitei, A. A. Zadpoor and N. A. Peppas, *Regener. Biomater.*, 2018, **5**, 197–211.
22 P. S. Lienemann, M. P. Lutolf and M. Ehrbar, *Adv. Drug Delivery Rev.*, 2012, **64**, 1078–1089.
23 Y. Xu, Y. Luo, Z. Weng, H. Xu, W. Zhang, Q. Li, H. Liu, L. Liu, Y. Wang, X. Liu, L. Liao and X. Wang, *ACS Nano*, 2023, **17**, 18732–18746.
24 F. F. Li, M. Gong, Y. N. Chen, X. H. Yang, L. Li, A. J. Chen, N. H. Dan and Z. J. Li, *Eur. Polym. J.*, 2024, **205**, 112755.
25 G. Bhakta, Z. X. H. Lim, B. Rai, T. Lin, J. H. Hui, G. D. Prestwich, A. J. van Wijnen, V. Nurcombe and S. M. Cool, *Acta Biomater.*, 2013, **9**, 9098–9106.
26 Y. Zhang, F. Zhao, J. Li, B. Yuan, X. Zhu, K. Zhang and X. Zhang, *Chem. Eng. J.*, 2024, **492**, 152402.
27 L. D. Pennington, B. M. Aquila, Y. Choi, R. A. Valiulin and I. Muegge, *J. Med. Chem.*, 2020, **63**, 8956–8976.
28 T. Huo, X. Zhao, Z. Cheng, J. Wei, M. Zhu, X. Dou and N. Jiao, *Acta Pharm. Sin. B*, 2024, **14**, 1030–1076.
29 X. Wang, X. Wu, H. Xing, G. Zhang, Q. Shi, L. E, N. Liu, T. Yang, D. Wang, F. Qi, L. Wang and H. Liu, *ACS Appl. Mater. Interfaces*, 2017, **9**, 11380–11391.
30 J. Li, F. Han, J. Ma, H. Wang, J. Pan, G. Yang, H. Zhao, J. Zhao, J. Liu, Z. Liu and B. Li, *Adv. Funct. Mater.*, 2021, **32**, 2111208.
31 S. Li, Y. Cui, H. Liu, Y. Tian, G. Wang, Y. Fan, J. Wang, D. Wu and Y. Wang, *J. Mater. Chem. B*, 2022, **10**, 9369–9388.
32 Z. Cai, H. Jiang, T. Lin, C. Wang, J. Ma, R. Gao, Y. Jiang and X. Zhou, *Mater. Today Adv.*, 2022, **16**, 100315.
33 T. Song, F. Zhao, L. Yan, P. Liu, J. Yang, C. Ruan, D. Li, Y. Xiao and X. Zhang, *Biomaterials*, 2024, **309**, 122601.
34 C. Martins, F. Sousa, F. Araújo and B. Sarmento, *Adv. Healthcare Mater.*, 2017, **7**, 1701035.
35 Y. Su, B. Zhang, R. Sun, W. Liu, Q. Zhu, X. Zhang, R. Wang and C. Chen, *Drug Delivery*, 2021, **28**, 1397–1418.
36 Z. Zhao, X. Ma, J. Ma, J. Kang, Y. Zhang and Y. Guo, *Mater. Today Bio*, 2022, **13**, 100206.
37 Y. Hua, Y. Su, H. Zhang, N. Liu, Z. Wang, X. Gao, J. Gao and A. Zheng, *Drug Delivery*, 2021, **28**, 1342–1355.
38 J. Yoo and Y.-Y. Won, *ACS Biomater. Sci. Eng.*, 2020, **6**, 6053–6062.
39 W. Chen, A. Palazzo, W. E. Hennink and R. J. Kok, *Mol. Pharmaceutics*, 2016, **14**, 459–467.
40 L. L. Lee, N. Niknafs, R. D. Hancocks and I. T. Norton, *Trends Food Sci. Technol.*, 2013, **31**, 72–78.
41 Y. Hu, Y. Yang, Y. Ning, C. Wang and Z. Tong, *Colloids Surf., B*, 2013, **112**, 96–102.
42 G. T. Vladisavljević, *Adv. Colloid Interface Sci.*, 2015, **225**, 53–87.
43 Y. Hu, J. Wang, X. Li, X. Hu, W. Zhou, X. Dong, C. Wang, Z. Yang and B. P. Binks, *J. Colloid Interface Sci.*, 2019, **545**, 104–115.
44 H. Zhang and A. I. Cooper, *Adv. Mater.*, 2007, **19**, 1529–1533.
45 C. M. Murphy, M. G. Haugh and F. J. O'Brien, *Biomaterials*, 2010, **31**, 461–466.
46 T. H. Qazi, J. Wu, V. G. Muir, S. Weintraub, S. E. Gullbrand, D. Lee, D. Issadore and J. A. Burdick, *Adv. Mater.*, 2022, **34**, 2109194.
47 Y. Hu, S. Cao, J. Chen, Y. Zhao, F. He, Q. Li, L. Zou and C. Shi, *Chem. Eng. J.*, 2020, **394**, 124895.
48 Q. L. Loh and C. Choong, *Tissue Eng., Part B*, 2013, **19**, 485–502.
49 C. Zhang, L. Yang, F. Wan, H. Bera, D. Cun, J. Rantanen and M. Yang, *Int. J. Pharm.*, 2020, **585**, 119441.
50 M. Zhang, A.-J. Wang, J.-M. Li, N. Song, Y. Song and R. He, *Mater. Sci. Eng., C*, 2017, **70**, 396–404.
51 B. Yan, X. Wang, X. Zhang, S. Liu, H. Lu and R. Ran, *Colloids Surf., A*, 2022, **639**, 128347.
52 Z. Liu, X. Li, B. Xiu, C. Duan, J. Li, X. Zhang, X. Yang, W. Dai, H. Johnson, H. Zhang and X. Feng, *Colloids Surf., B*, 2016, **145**, 679–687.

53 H. Lei, J. Shi, X. Yang, J. Li, H. Zhang, L. Zhang and Z. Liu, *J. Pharm. Innovation*, 2020, **16**, 620–629.
54 N. Venkatesan, A. D. T. Liyanage, J. Castro-Núñez, T. Asafo-Adjei, L. L. Cunningham, T. D. Dziubla and D. A. Puleo, *Acta Biomater.*, 2019, **93**, 192–199.
55 X. Zhang, J. Fan, C. Chen, T. Aghaloo and M. Lee, *J. Mater. Chem. B*, 2021, **9**, 7741–7750.
56 H. Jin, Y. Ji, Y. Cui, L. Xu, H. Liu and J. Wang, *ACS Biomater. Sci. Eng.*, 2021, **7**, 2177–2191.
57 F. Wu, G. Meng, J. He, Y. Wu, F. Wu and Z. Gu, *ACS Appl. Mater. Interfaces*, 2014, **6**, 10005–10013.
58 M. G. N. Campos, H. R. Rawls, L. H. Innocentini-Mei and N. Satsangi, *J. Mater. Sci.: Mater. Med.*, 2008, **20**, 537–542.
59 Y. Wang, W. Yu, C. Niu, G. Yu, X. Huang, J. Shi, D. Ma, X. Lin and K. Zhao, *Polym. Test.*, 2022, **116**, 107762.
60 T. Jiang, R. R. Petersen, G. Call, G. Ofek, J. Gao and J. Q. Yao, *J. Biomed. Mater. Res., Part B*, 2011, **97B**, 355–363.
61 J. Siepmann, N. Faisant, J. Akiki, J. Richard and J. P. Benoit, *J. Controlled Release*, 2004, **96**, 123–134.
62 Q. Xu, M. Hashimoto, T. T. Dang, T. Hoare, D. S. Kohane, G. M. Whitesides, R. Langer and D. G. Anderson, *Small*, 2009, **5**, 1575–1581.
63 L. Ruan, M. Su, X. Qin, Q. Ruan, W. Lang, M. Wu, Y. Chen and Q. Lv, *Mater. Today Bio*, 2022, **16**, 100394.
64 M. Vallet-Regí, D. Lozano, B. González and I. Izquierdo-Barba, *Adv. Healthcare Mater.*, 2020, **9**, 2000310.

